Dehydration as a Universal Mechanism for Ion Selectivity in Graphene and Other Atomically Thin Pores – Supporting Information

Subin Sahu,[1,2,3] Massimiliano Di Ventra,[4] and Michael Zwolak[1]

[1]*Center for Nanoscale Science and Technology, National Institute of Standards and Technology, Gaithersburg, Maryland 20899*

[2]*Maryland Nanocenter, University of Maryland, College Park, Maryland 20742*

[3]*Department of Physics, Oregon State University, Corvallis, Oregon 97331*

[4]*Department of Physics, University of California, San Diego, California 92093*

CONTENTS

I. METHODS

A. Molecular Dynamics

Graphene has carbon atoms located at the points $\hat{r}_{nm} = m\hat{a}_1 + n\hat{r}_2$ for m, $n \in \mathbb{Z}$, where $\hat{a}_1 = a(3, \sqrt{3})/2$ and $\hat{a}_2 = a(3, -\sqrt{3})/2$ are the 2D lattice vectors and $a \approx 0.14$ nm is the C-C bond length. We open a pore of nominal radius r_n at the center of each membrane by removing carbon atoms satisfying the condition $x^2 + y^2 < r_n^2$, with x, y the coordinates of the atom in the $z = 0$ plane. We then immerse the membrane in an aqueous ionic solution, typically with 1 mol/L salt concentration, consistent with experiments. We use the CHARMM27 force field to model the atoms. The carbon atoms are type CA and water molecules are TIP3P from the CHARMM27 force field.

We perform all-atom molecular dynamics (MD) simulations using NAMD [1] with a time step of 1 fs and periodic boundary conditions in all directions. We use a cutoff of 1.2 nm for non-bonded interactions, i.e., van der Waals and electrostatics. However, we use full electrostatic calculations every 4 fs via the particle-mesh Ewald (PME) method [2]. We first minimize the energy of the system for 4000 steps (4 ps) and then heat it to 295 K in another 4 ps. A 0.5 ns NPT (constant number of particles, pressure and temperature) equilibration using the Nose-Hoover Langevin piston method [3] – to raise the pressure to 101 325 Pa (i.e., 1 atm) – followed by 1.5 ns of NVT (constant number of particles, volume and temperature) equilibration generates the initial atomic configuration. An electric field perpendicular to the plane of the membrane drives the ionic current through the pore. We set the Langevin damping rate to 0.2/ps for carbon and water (via its oxygen atoms) during these runs. Test runs show that damping the hydrogen atoms does not affect the results. Damping the ions, however, affects the current as it changes the ionic mobility.

We fix the outer edge of the graphene membrane, but the bulk of the membrane has no confinement other than the C-C bonds of graphene. The production runs vary from 100 ns to 1.1 μs based on the convergence of the current and other properties of interest. When calculating the water density around an ion fixed at the origin (e.g., in the center of the pore when it is not fluctuating), the parameters are the same except there was no external electric field present.

We use the adaptive biasing force method (ABF) [4, 5] in the colvar module of NAMD

to perform the free energy calculation. In this method the reaction coordinate, ζ (z for the setup here), is divided into equally spaced bins and the free-energy difference along ζ is calculated by integrating the equation

$$\langle f_\zeta \rangle_k = -\left\langle \frac{\partial U(X)}{\partial \zeta} - \frac{\partial ln|J|}{\partial \zeta} \right\rangle_k \equiv -\frac{dF(k)}{d\zeta}, \tag{1}$$

where $\langle f_\zeta \rangle_k$ and $F(k)$ are the mean force and free energy at bin k, X are the cartesian coordinates, and $|J|$ is the Jacobian of the transformation to cartesian coordinates. The ABF method applies an iterative biasing force, $\bar{f}_n(k)$, which is the average of all force samples after n MD steps in the bin k. This force enables the system to overcome free-energy barriers during an unconstrained MD run and allows for a more uniform sampling along the reaction coordinate. In our simulation, we calculate the one-dimensional free energy profile along the z-axis in bins of width 0.01 nm from $z = -1.5$ nm to $z = 1.5$ nm. We perform ABF calculation on three windows, (-1.5 nm $\leqslant z \leqslant -0.5$ nm), (-0.5 nm $\leqslant z \leqslant 0.5$ nm), and (0.5 nm $\leqslant z \leqslant 1.5$ nm), and also symmetrize the final result about $z = 0$ for better sampling. Also, we confine the ion within a cylinder of radius 0.2 nm centered at the origin, where a bounding potential with force constant ≈ 43 eV/nm^2 turns on outside of the 0.2 nm cylinder. In each bin, 800 samples of the instantaneous force are accrued prior to the full application of the ABF. This biasing force scales up linearly by a factor of 0 to 1 from 400 samples to 800 samples, and no biasing force is applied below 400 samples. The total simulation consists of about 120 runs of 10 ns each for each window.

We use the block standard error (BSE) method [6] to compute the error bars for all plots. The BSE is given by

$$\text{BSE} = \frac{s_\tau \sqrt{\tau}}{\sqrt{T}}, \tag{2}$$

where T is the total simulation time (the time of the MD trajectory), τ is a length of time used to partition the simulation into many contiguous blocks, and $s_\tau = \sqrt{\frac{\sum_i (\langle I_\tau \rangle_i - \langle I_T \rangle)^2}{(N_b - 1)}}$ is the standard deviation of the mean current, $\langle I_\tau \rangle$, within each of the N_b blocks. The BSE depends on τ when the latter is very small (i.e., when τ is smaller than the timescale required to get independent reads of the current) or very large ($\tau \approx T$). In the first case, the dependence is due to the fluctuations in the mean being correlated and, in the later case, the estimate of the standard deviation having too few data points. However, the BSE is fairly constant over a broad range of τ in between, which is the value we used to estimate errors. The error bars in the plots are ± 1 BSE unless otherwise indicated.

B. Pore radius and area

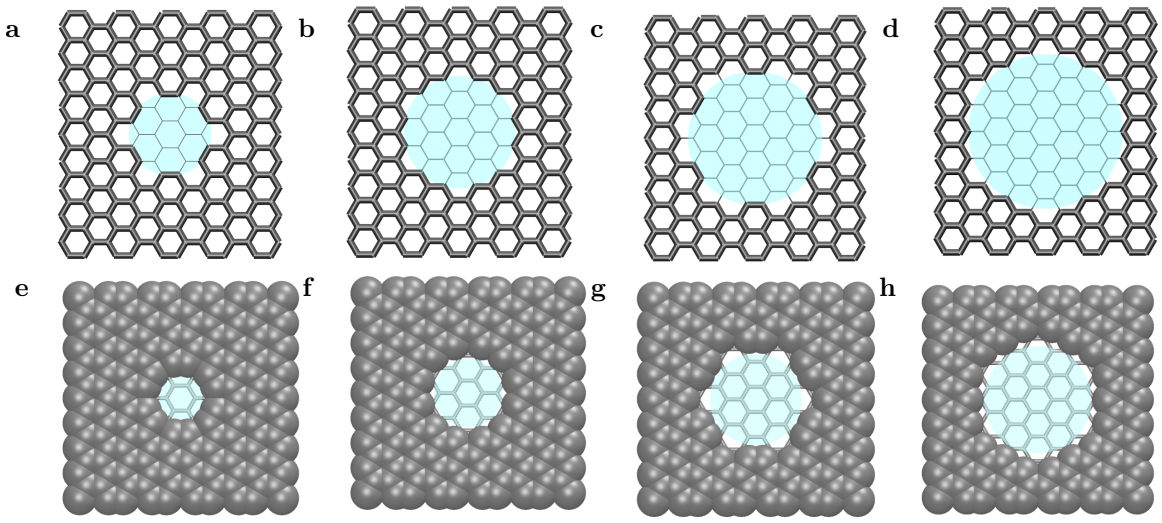

FIG. S-1. Membrane and pore structure. The images show a small section of the graphene membrane (2.1 nm by 2.1 nm) containing the pore. (a-d) The top panels show the nominal radii, $r_n = 0.38$ nm, 0.51 nm, 0.62 nm, and 0.71 nm. (e-h) The bottom panels show the corresponding effective radii, $r_p = 0.21$ nm, 0.34 nm, 0.45 nm, and 0.54 nm.

r_n (nm)	0.38	0.51	0.62	0.71	0.86	0.93	1.11	1.24	1.36	1.48
r_p (nm)	0.21	0.34	0.45	0.54	0.69	0.76	0.94	1.07	1.19	1.31

TABLE S-1. Radii for various pores. Here, r_n is the nominal radius of the pore (it defines the construction of the pore for the simulations) and $r_p = r_n - \sigma_C$ is the effective radius, where σ_c is the vdW radius of carbon. The quantity $r_p = r_n - \sigma_C$ also gives the radius that would be observed in experiments due to electron density around the carbon atoms and bonds.

As noted above, we open pores by removing carbon atoms with coordinates satisfying $x^2 + y^2 < r_n^2$. There is a range of r_n that give the same pore size due to the discrete nature of the membrane. We choose r_n to be the maximum of this range. This r_n also gives the distance of the carbon atoms at the pore edge to the center of the pore, see Fig. S-1 (in other words, the radius of the largest circle that will fit into the pore).

When comparing to experimental results, however, these nominal radii may or may not correspond to the values reported. For instance, Ref. 7 defines the pore area by where

electron density is not observed in transmission electron microscopy (TEM) images. This will roughly correspond to $r_n - \sigma_C$ where $\sigma_C \approx 0.17$ nm is the van der Waals (vdW) radius of carbon. This is approximately where the electron density vanishes. Moreover, the actual area available for transport is smaller than nominal area due to hydration and the finite size of atoms (note, however, that the flexibility of the pore edge will tend to slightly increase the area available). These factors have negligible effect in larger pores but are significant for subnanoscale pores. We found that in general the maximum radial spread of the ion inside the pore is given by: $\rho_{max} \approx r_n - \sigma_C$ (see Fig. S-2). Thus, we define the effective pore radius as $r_p = r_n - \sigma_C$ and effective area of the pore as $A_p = \pi r_p^2$. This definition should roughly correspond to experimentally observed values. We note that to find the actual accessible area for transport, one should also account for the spatial dependence of the free energy. Table S-5 reports the nominal and effective radii.

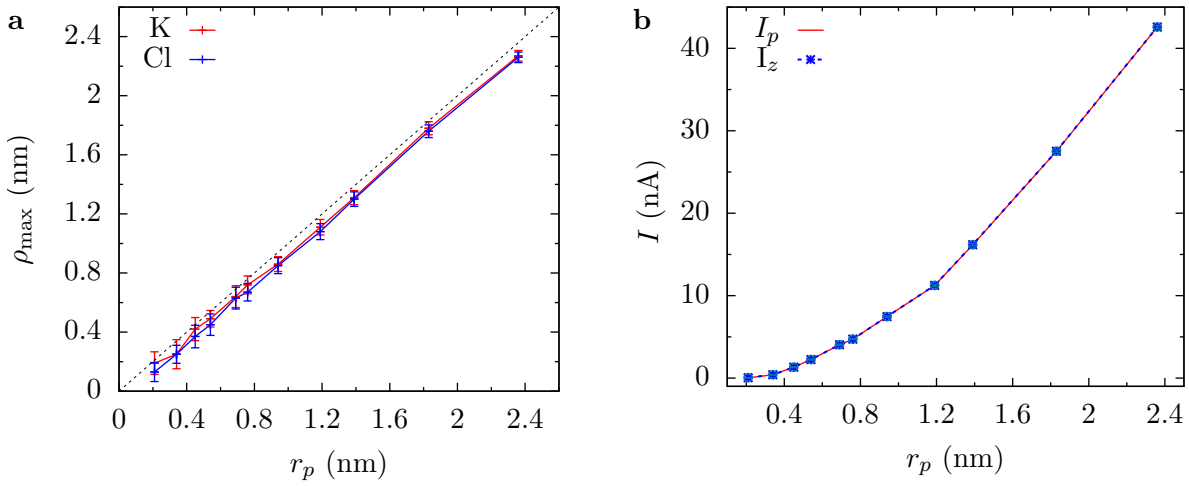

FIG. S-2. Transport area and current definition. (a) The maximum (cutoff of 99 %) radial spread ($\rho^2 = x^2 + y^2$) of ions inside the pore is roughly equal to r_p nm. That is, when looking at the integrated density of translocation events from 0 to ρ, 99 % of the events fall between 0 and ρ_{max}. (b) Current calculated from the two different definitions I_p (solid line) and I_z (dashed line). Connecting lines are shown as a guide to the eye.

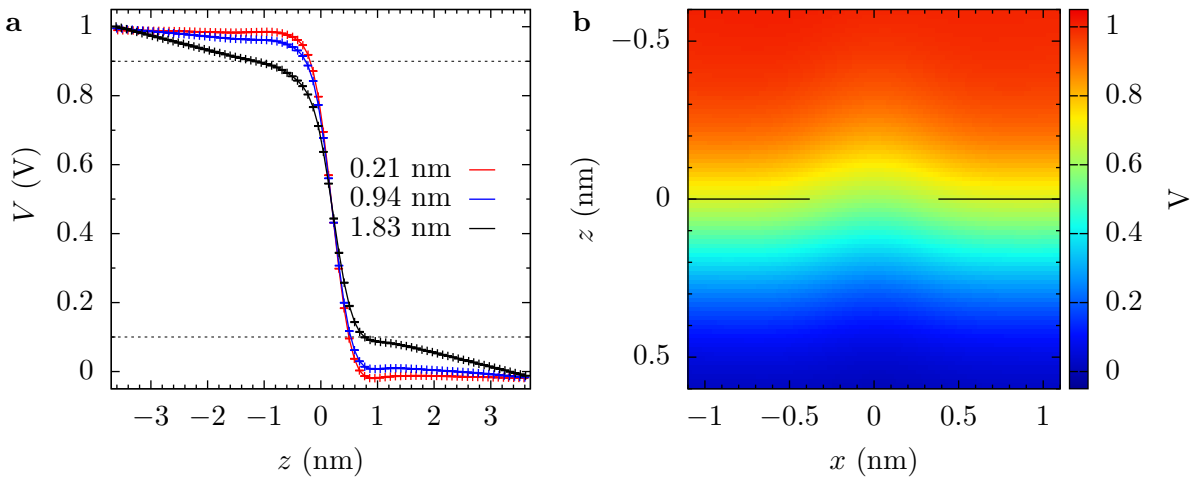

FIG. S-3. Voltage drop. (a) Potential drop along the z-axis for various pore sizes and (b) a map of the potential for a pore of radius 0.21 nm. For larger pores, most of the potential drop (about 80% shown by the two dotted horizontal lines) occurs within a distance r_p from the center of pore. The electric field can thus be approximated by $E \approx 0.8\,V/2r_p$. However, for small pores, the entire potential drop occurs over 1 nm due to vdW repulsion of the ions by the graphene membrane. In Fig. 2 of the main text, we use the approximate electric field for larger pores in the expression $ez_\nu n_\nu \mu_\nu A_p E$ for the whole range of values reported. This overestimates the field for smaller pores, but will approach the right value as the pore size increases. Note, as well, that K^+ tends to come closer to the graphene membrane due to its smaller vdW repulsion. This results in the potential drop occurring mostly on the anion side and, when the voltage is increased enough to substantially polarize water, in the effective barrier for K^+ decreasing before that for Cl^-. Connecting lines are shown as a guide to the eye. The potential maps were produced using the method described in Ref. 8.

C. Current definition and electric field

The ionic current was calculated using two definitions:

$$I_z(t) = \frac{1}{\Delta t L_z} \sum_{i=1}^{N} q_i [z_i(t + \Delta t) - z_i(t)], \tag{3}$$

and

$$I_p(t) = \frac{1}{\Delta t} \sum_{i=1}^{N} q_i (\Theta[Z_i(t + \Delta t)] - \Theta[Z_i(t)]), \tag{4}$$

where Θ is the Heaviside step function and $\Delta t = 1$ ps is the measurement time (we record the atomic configuration every Δt increment). The first definition takes into account the motion of all ions in the z-direction and the second definition counts ions crossing the pore. These definitions give the same value for the current so long as the simulation is converged with respect to the total simulation time (see Fig. S-2(b)).

We found that about 80 % of the potential drops within a sphere of radius r_p from the center of the pore for larger pores (see Fig. S-3). Thus, the electric field inside the pore can be estimated as $E \approx 0.8\,V/2r_p$. For the smallest pore, however, the electric field is more accurately determined by $E \approx V/L$ with $L = 1$ nm. This is because vdW repulsion of the ions by the carbon prevents the charge layers from getting closer than about 1 nm.

We tested the effect of box size on the current by comparing different box sizes, a large box (with fixed cross-sectional area 7.4 nm $\times$ 7.4 nm and relaxed height 6.9 nm), a small box (with fixed cross-sectional area 3.7 nm $\times$ 3.7 nm and relaxed height 3.4 nm), and a extended small box (with fixed cross-sectional area 3.7 nm $\times$ 3.7 nm and relaxed height 6.9 nm). The current and selectivity are in agreement (to within the errors reported) for all box sizes when the pore is small and at low voltages, as the current is dominated by the high pore resistance. The latter allows well-defined charge layers to develop and persist. However, for larger pores, the current was smaller by about 20 % for the larger box size. Since both box sizes have the same voltage and same concentration of ions, the difference in current is likely due to a smaller access resistance and lack of well-defined charge layers in the boxes with smaller cross-sectional area, as the pore diameter approaches the edge of the box. For the smallest pore size calculations, we use the extended small box, as it considerably reduces errors due to convergence in time, i.e., we can run microsecond long simulations, which are necessary when the currents are so small.

II. CURRENT BEHAVIOR AT THE SUBNANOSCALE

The ionic current begins to show abnormal behavior as the radius of the pore decreases to the sub-nanometer scale. This behavior is seen in the sharp rise in the pore resistance and noise in the current, Fig. S-4. At these length scales, the pore edge begins to deform the hydration layers around the ions, which increases the energy barrier for ions to cross the pore.

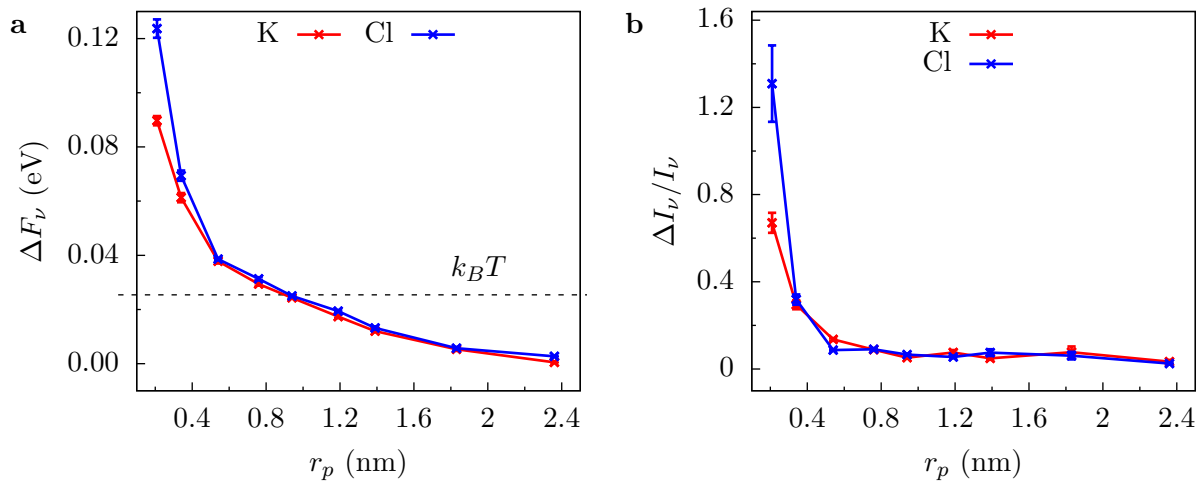

FIG. S-4. Estimates of the free energy barrier and noise for various pores. Sharp rise in (a) the free energy barrier and (b) the noise in the current at the subnanoscale. An "average" free energy barrier is estimated as $\Delta F_\nu = k_B T \log\left(\frac{q_\nu n A_p \mu_\nu E}{I_\nu}\right)$, where q_ν, μ_ν, n are the charge, average mobility (of K^+ and Cl^-), and particle concentration. The error in ΔF_ν is thus $k_B T \delta I_\nu / I_\nu$, where δI_ν is BSE in I_ν. The noise in current, $\Delta I_\nu(\tau)$ is measured by standard deviation of the mean current within blocks of length $\tau = 10$ ns. The relative noise in the current, $\Delta I_\nu(\tau)/I_\nu$ increases sharply due to the fluctuations in hydration layer configurations that allow or prohibit passage of ions through the pore [9]. The errors in ΔI_ν is estimated as $\frac{\Delta I_\nu}{\sqrt{2(N_b-1)}}$ [10]. Connecting lines are shown as a guide to the eye.

III. SELECTIVITY

A. Experimental observation of selectivity

Ref. 7 found that graphene membranes with a distribution of pore sizes (at the sub-nanoscale) display selective behavior for K^+ over Cl^-. In that work, this is indicated by a nonzero membrane potential E_m. We use the relation

$$E_m = \frac{k_B T}{e} \ln\left(\frac{P_K[K]_o + P_{Cl}[Cl]_i}{P_K[K]_i + P_{Cl}[Cl]_o}\right) \tag{5}$$

or, rearranging,

$$e^{eE_m/k_BT} = \frac{\frac{P_K}{P_{Cl}}[K]_o + [Cl]_i}{\frac{P_K}{P_{Cl}}[K]_i + [Cl]_o} \tag{6}$$

to estimate the selectivity from the reported membrane potential ($E_m = 3.3$ mV ± 1 mV, where we keep the second digit to not introduce rounding error, $[K]_i = [Cl]_i = 0.17$ mol/L,

A_p (nm^2)	0.2	0.123	0.108	0.321	0.368
r_p (nm)	0.25	0.20	0.19	0.32	0.34
S_p	S	S	S	1	1

TABLE S-2. Current-carrying pores from the selectivity measurement of Ref. 7. We assign a selectivity S for all pores with $r_p \approx 0.2$ nm and 1 for larger pores. There are also many pores with smaller radii, but we expect these pores to carry negligible current (and thus, even though they will be selective, they do not contribute to the observed selectivity). We do not include them in this table.

$[\mathrm{K}]_o = [\mathrm{Cl}]_o = 0.5$ mol/L , $T = 297$ K, and e is the magnitude of the electron charge). We obtain $\tilde{S} = P_\mathrm{K}/P_\mathrm{Cl} = 1.3 \pm 0.1$ as an "average" selectivity for their distribution of pore sizes. The ratio $P_\mathrm{K}/P_\mathrm{Cl}$ is the concentration-imbalance equivalent of $I_\mathrm{K}/I_\mathrm{Cl}$.

To compare with our numbers, we need to extract the selectivity for particular pore sizes or to use the MD results to compute the average for the distribution of pore sizes in experiment. We will do both. We first note that the average selectivity from experiment is the same as the selectivity we find for $r_p = 0.34$ nm (see Fig. 2 in the main text and Table S-7). Although the experimental selectivity is for the distribution of pore radii from $r_p \approx 0.1$ nm to $r_p \approx 0.3$ nm, it is likely that most of the current and hence the average selectivity is dominated by pores with $r_p \approx 0.3$ nm. In fact, we find that current for $r_p = 0.34$ nm is an order of magnitude larger than that for $r_p = 0.2$ nm, supporting that the slightly larger pore may be dominating the average.

To go further, though, we will first use a rough estimate to extract the selectivity for the $r_p \approx 0.2$ nm from experiment and then separately show that, when using the areas and free energies from our MD calculations, we get an average selectivity similar to experiment. Both of these calculations confirm that dehydration-only selectivity yields results in agreement with experiment.

For a membrane with a distribution of pore sizes, the observed selectivity $\tilde{S}$ can be roughly estimated as

$$\tilde{S} = \frac{\sum_p I_{pK}}{\sum_p I_{pCl}} = \frac{\sum_p S_p I_{pCl}}{\sum_p I_{pCl}} \approx \frac{\sum_p S_p A_p}{\sum_p A_p} \tag{7}$$

or

$$\tilde{S} = \frac{\sum_p I_{pK}}{\sum_p I_{pCl}} = \frac{\sum_p I_{pK}}{\sum_p (1/S_p) I_{pK}} \approx \frac{\sum_p A_p}{\sum_p (1/S_p) A_p}, \tag{8}$$

Salt (XCl)	CsCl	RbCl	KCl	NaCl	LiCl
σ (pS)	67	70	64	42	27
κ (10^{-3} S m^{-1})	1.42	1.42	1.3	1.19	0.95
E_X (eV)	3.1	3.4	3.7	4.6	5.7
μ_X (10^{-8} m^{2}V^{-1}s^{-1})	8.01	8.06	7.62	5.19	4.01
μ_{eff} (10^{-8} m^{2}V^{-1}s^{-1})	4.25	3.59	4.29	1.63	1.03
σ_{XCl} (pS)	67	61-67	65-67	44-55	39-50
σ_X (pS)	67	57-66	64-68	26-43	16-34

TABLE S-3. Leakage conductance (σ), bulk conductivity of cations and anions together (κ), and hydration energy (E_X) of the cation X, as reported by Ref. 11. Note that the reported bulk conductivity is four orders of magnitude smaller than that in their nanopore current measurements. We take the cation mobilities (μ_X) from bulk [12] and effective cation mobilities (μ_{eff}) in a biological pore from Ref. 13. The bulk mobility of Cl^- ion is 7.92×10^{-8} m^{-2} V^{-1} s^{-1} and its effective pore mobility (from Ref. 13) is 3.44×10^{-8} m^{-2} V^{-1} s^{-1}. We make two estimates of the range of the conductance: One for σ_{XCl} (assuming both the cation and anion contribute) and the other for σ_X (assuming only the cation contributes). The range in each case is set by the bulk mobility and the effective pore mobility. We note that even though graphene is atomically thick (and effective mobilities are not well defined), the defect channel structure is not known – those channels could be long channels through gaps in the device. We use the effective mobilities of Ref. 13 for a biological pore only as a very rough estimate. These ranges show that the deviation of the relative conductance from that predicted by bulk mobilities can easily be due to cation-only conductance (e.g., due to local charge-based selectivity) and/or effective mobilities through the defect channels responsible for the leakage conductance. Note that the conductance of CsCl and Cs only in the last two lines are the same. This is because they are assuming two different hypotheses about the origin of the conductance and we take them both to be the experimentally determined conductance. Also, for clarity, the estimated range is color coded with blue indicating the estimate using the bulk mobility and red the estimate from the effective mobility.

where S_p (A_p) is the selectivity (area) for a pore of radius r_p and the sum over p goes over individual pores. The approximate expressions in each equation assume that the current is proportional to area, but without a free energy barrier (see below for the average computed

cation(X)	K^+	Li^+	Ba^{2+}	Ca^{2+}	Mg^{2+}
μ_X (10^{-8} $m^2V^{-1}s^{-1}$)	7.62	4.01	6.60	6.17	5.50
	device 3, $r_p = (0.36 \pm 0.10)$ nm				
σ (nS)	2.3 ± 1.2	1.1± 1.1	1.0±0.8	0.7± 0.5	0.4± 0.03
$S_{XCl/KCl}$	1	0.00 - 2.61	0.06 - 1.75	0.06 - 1.25	0.11 - 0.41
$S_{X/K}$	1	0.00 - 3.80	0.07 - 1.89	0.07 - 1.40	0.13 - 0.49
	device 4, $r_p = (0.50 \pm 0.10)$ nm				
σ (nS)	4.2 ± 0.3	2.2± 1.3	1.4 ±0	1.5±0.1	1.3± 0.1
$S_{XCl/KCl}$	1	0.25 - 1.17	0.34 - 0.40	0.34 - 0.45	0.31 - 0.39
$S_{X/K}$	1	0.37 - 1.71	0.37 - 0.43	0.38 - 0.51	0.37 - 0.46
	device 8, $r_p = (0.39 \pm 0.06)$ nm				
σ (nS)	2.6±1.5	1.3±0.1	2.3±1	2±1	1±1
$S_{XCl/KCl}$	1	0.39 - 1.65	0.32 - 3.21	0.28 - 3.01	0.00 - 2.00
$S_{X/K}$	1	0.57 - 2.42	0.35 - 3.46	0.31 - 3.37	0.00 - 2.39

TABLE S-4. Chloride salt conductance (σ) of three different devices holding the chloride concentration constant at 100 mM [14]. The quantity $S_{XCl/KCl}$ is the selectivity quantified by assuming both cation and anion contribute, Eq. 12, and $S_{X/K}$ by assuming only cations contribute, Eq. 13. The selectivity is shown as a range based on the error in σ (the actual range – the range of the data measured in Ref. 14 – is larger than shown here). Only bivalent ions in device 4 and Mg^{2+} in device 3 potentially show selective behavior. However, selectivity of this magnitude was observed in Ref. 15 for large pores, where dehydration can not be playing a role.

with free energy barriers). This is a strong approximation. It requires, at the least, that the smallest pore sizes (i.e., with radii of about 0.15 nm and below) to be dropped from the sum (as their current contribution is negligible and not necessarily proportional to area). The sum is thus over the data in Table S-2, which is from the selective membrane (5 min etch time) of Ref. 7. This gives $S = 1.8 \pm 0.3$ from Eq. (7) and $S = 2.5 \pm 1$ from Eq. (8), where we again keep the second digit to not introduce rounding error. The difference in the selectivity estimated from the two equations is due to the fact that they did not take into account the free energy barrier at smaller radii. The error is calculated based on the error in $\tilde{S}$ only, as the error in area is not reported in Ref. 7. However, the error due to area is

expected to be much smaller than the approximations in the equations. In the main text, we report the range 1.8 to 2.5 for the selectivity of the $r_p \approx 0.2$ nm pores.

A more accurate calculation requires the value of free energy barrier and selectivity for each of the pores in the distribution. We can, however, estimate the average selectivity for their pore size distribution (Table S-2) using the free-energy barriers in Fig S-4,

$$\tilde{S}_{\text{estimate}} = \frac{\sum_p I_{pK}}{\sum_p I_{pCl}} = \frac{\sum_p \mu_{\text{K}} A_p e_p^{-\Delta F_{\text{K}}/K_B T}}{\sum_p \mu_{\text{Cl}} A_p e_p^{-\Delta F_{\text{Cl}}/K_B T}} \approx 1.5, \tag{9}$$

which is very close to the ≈ 1.3 result from experiment. Here, we again dropped the smallest pores (ones smaller than $r_p \approx 0.2$ nm) from the average, as the free energy barrier will be more substantial and suppress their contribution to the selectivity.

We note a few important limitations of this comparison between the experiments and our calculations. The lowest voltage in our simulations is still order of magnitude larger than the equivalent chemical potential difference in the experiments. The regime below 0.25 V is very difficult to reach using all-atom MD simulation for these pore sizes. Moreover, current experimental techniques cannot control the functionalization of graphene nanopores (and functionalization/surface species of the graphene membrane) which depends on the fabrication method and other factors. Since it is not clear what groups will be present and where, we choose the simplest pore – the one with no functionalization. As well, some functionalization will introduce charges/dipoles to the pore region. However, if these are close (either on the pore rim or nearby), they will not give rise to the weak selectivity observed, but rather a strong selectivity, unless the charge is very small in magnitude.

Garaj et al. [11] report that the leakage current (the current through a graphene membrane when the pores have yet to be constructed) deviates from what the bulk conductivity would predict, which they conjecture may be due to dehydration. Taking the experimental conductance of CsCl to be the reference value, we can estimate the conductance of other salts XCl as

$$\sigma_{\text{XCl}} = \frac{\sigma_{\text{CsCl}}}{(\mu_{\text{Cs}} + \mu_{\text{Cl}})}(\mu_{\text{X}} + \mu_{\text{Cl}}). \tag{10}$$

As shown in Table S-3, the difference in *effective* mobilities of ions inside of pores explains some of the deviation. In fact, since the leakage conductance varies widely from membrane to membrane (by a factor of two [11]), different effective mobilities alone may explain the deviation to within experimental uncertainties.

An alternative (or complementary) explanation is that the defect channels – the structure of which is unknown – are cation selective due to the presence of negative (partial) charges. In this case, the estimated conductance is

$$\sigma_{\mathrm{X}} = \frac{\sigma_{\mathrm{Cs}}}{\mu_{\mathrm{Cs}}}\mu_{\mathrm{X}}. \tag{11}$$

This estimate accurately explains the observations by itself. Relying on dehydration requires a convoluted explanation – or minuscule dehydration, e.g., a $1/100^{\mathrm{th}}$ fractional removal of water – to account for the differences between K^+, Na^+, and Li^+ when comparing to Cs^+. For instance, Na^+ and Li^+ have a much larger hydration energies than Cs^+, Rb^+, or K^+, and thus one expects that, if dehydration is a factor, the membrane conductance would go from cation and anion both contributing (for Cs^+, Rb^+, and K^+) to just anion contributing (for Na^+ and Li^+). In other words, NaCl and LiCl would have the same conductance, but they differ by 50 %.

We also note that ion transport for different cations was measured in Ref. 14, where the authors claim to have observed hydration-based selectivity. However, their selectivity can be explained based on difference in cation mobilities. Selectivity with respect to KCl can be captured via the normalized conductance

$$S_{\mathrm{XCl/KCl}} = \frac{\sigma_{\mathrm{XCl}}/(\mu_{\mathrm{X}} + \mu_{\mathrm{Cl}})}{\sigma_{\mathrm{KCl}}/(\mu_{\mathrm{K}} + \mu_{\mathrm{Cl}})}. \tag{12}$$

As shown in Table S-4, the selectivity has a large range due to a large variation of the conductance. This makes it difficult to determine if there is any selectivity at all. Only the bivalent ions in device 4 and Mg^{2+} in device 3 have the entire range of $S_{\mathrm{XCl/KCl}}$ less than 1. Moreover, the experimental results seem to indicate the presence of negative charges near the pore (see Fig. 3d in Ref. 14), which would mean that most of the current is carried by the cations. Thus, selectivity should be quantified as

$$S_{\mathrm{X/K}} = \frac{\sigma_{\mathrm{XCl}}/\mu_{\mathrm{X}}}{\sigma_{\mathrm{KCl}}/\mu_{\mathrm{K}}}. \tag{13}$$

This shows that (12) overestimates the deviation from non-selective behavior. As we mention in the main text, even if one ignores the large variation in the measured conductance in individual devices (and from device to device), the selectivity reported is consistent with the charge-based selectivity observed in Ref. 15. Those latter results were in pores much bigger than hydrated ions, indicating that the selective behavior is likely due to differences in how

bivalent versus monovalent ions screen the charged pore/membrane. We finally note that the difference in hydration energy of monovalent and divalent ions is around 10 eV. It seems unlikely that this would give selectivity on the order of a factor of 2.

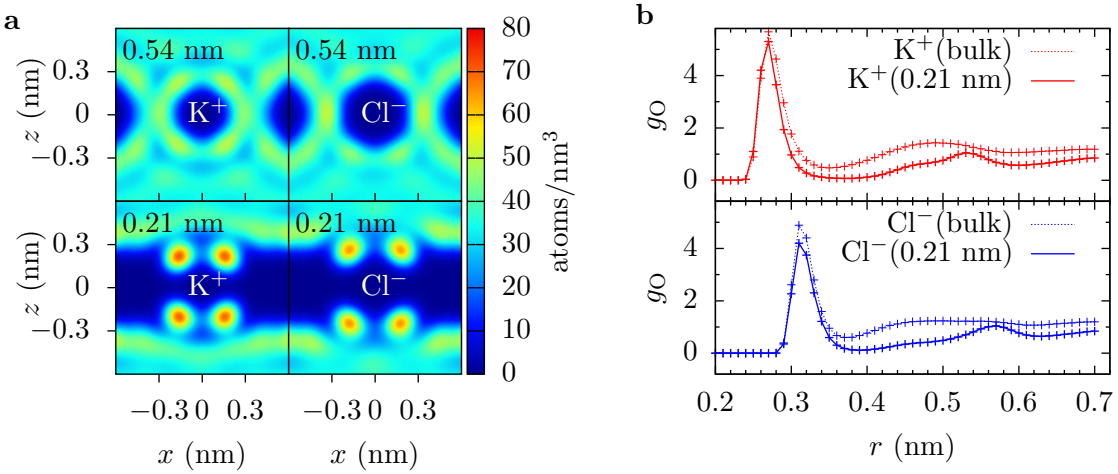

FIG. S-5. Water density quantified by the oxygen density. (a) The contour plots show either a potassium or a chloride ion fixed at the center of the pore. The pore radius is shown in the upper left corner of each panel. The hydration layers are visible as the high-density region around the ion. As the pore size gets smaller, the hydration layers around the ion are distorted by the pore edge. The ions remain fairly well hydrated. (b) The radial distribution function of oxygen atoms around K^+ and Cl^- in bulk and at the center of a $r_p = 0.21$ nm pore (with a counter ion fixed at the edge of the simulation cell) for zero bias showing partial dehydration. The number of water molecules in first hydration layer of K^+ and Cl^- are 6.8 and 7.4 in bulk and 5.2 and 5.8 at the center of pore, respectively, i.e., a loss of about 1/4 of the water molecules from first hydration layer. Connecting lines are shown as a guide to the eye.

B. Dehydration and selectivity

Figure S-5 shows the water density around the ion in the pore and the radial distribution function of oxygen, g_O. In our simulation, the number of oxygen atoms in first hydration layer around K^+ and Cl^- in bulk water are 7.4 and 6.8, respectively, and, when placed in the center of a $r_p = 0.21$ nm pore, 5.8 and 5.2. This is loss of about 1/4 of the water molecules from the innermost layer. Even though the fractional dehydration for K^+ and Cl^-

are nearly equal, the energy penalty is higher for Cl^- as its inner hydration layer is more strongly bound compare to K^+. As we increase the applied voltage, both ions were able to remain more hydrated while crossing the pore due to polarization-induced chaperoning of the ions. This results in a lower free energy barrier for transport, as seen from Fig. S-6.

IV. MODEL FOR ION TRANSPORT

The model for ion transport is discussed in detail in the main text. We use the method of least squares, with the first data voltage point constrained to reflect behavior at lower voltage, to fit the data. We only present data up to 1.5 V in the main text as water starts to dissociate at high fields. However, all-atom MD simulations allow us to apply much higher voltages without dissociating water. We thus looked at the IV characteristics up to 3 V to check consistency with our model, which fits well up to that voltage when accounting for a change in free energy barrier for Cl^-, as seen in Fig. S-6.

V. THE EFFECT OF THE ION CONCENTRATION

In order to confirm that the anomalous behavior of current and weak selectivity is not due to a many-body effect but rather to single ion behavior, we repeat the selectivity calculations for lower concentrations of KCl. Both the anomalous behavior of current and weak selectivity are still present in concentrations as low as 0.1 mol/L, at which point there were only a few ions of each type in the smallest simulation box size (hence, box size errors start to become significant).

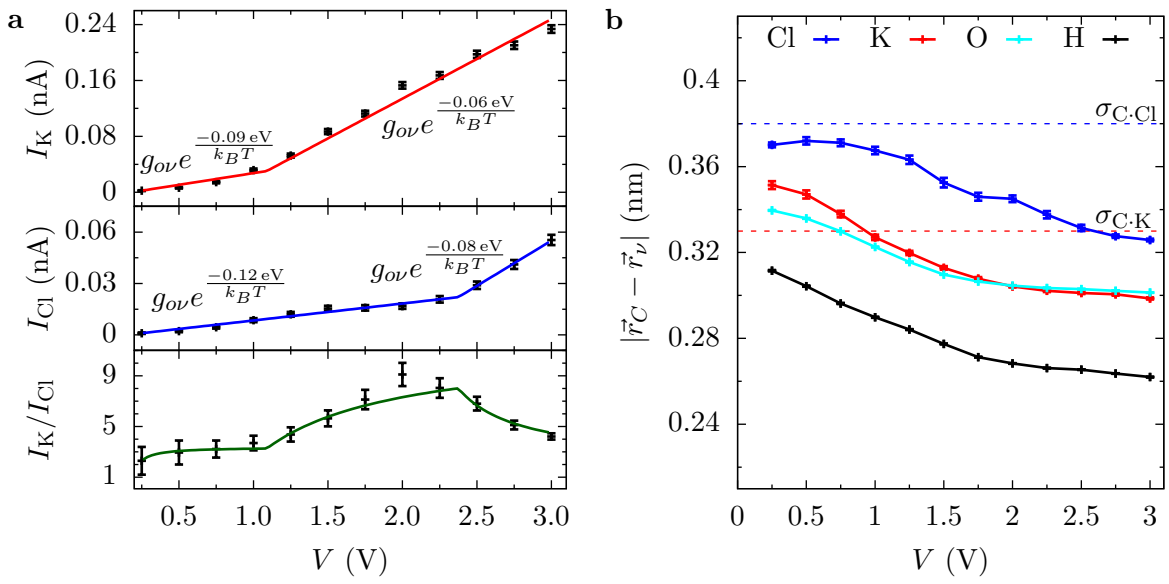

FIG. S-6. Model for ion transport. (a) Current-voltage characteristics for a pore of radius 0.21 nm and 1 mol/L KCl versus voltage (top panels). The relative selectivity of K^+ over Cl^- in the same pore (bottom panel). Data points give the MD results and the solid line gives the piece-wise linear model we fitted taking each region to be linearly related to the differential conductance $g_\nu = ez_\nu n_\nu e^{(-\Delta F_\nu/k_BT)}\mu_\nu A_p/L = g_{0\nu}e^{(-\Delta F_\nu/k_BT)}$. Around (1.1 ± 0.1) V the energy barrier for potassium drops from (0.09 ± 0.004) eV to (0.06 ± 0.002) eV, whereas that of chloride drops from (0.12 ± 0.001) eV to (0.08 ± 0.008) eV around (2.38 ± 0.04) V. This change in conductance with voltage results in a rise and fall of selectivity. (b) The distance ($|\vec{r}_C - \vec{r}_\nu|$) between an ion ν (or an oxygen/hydrogen from water) crossing the pore and the nearest carbon atom versus voltage. At higher voltage ions are able to apparently enter the repulsive zone ($r < \sigma$) of vdW potential of carbon atom, likely due to larger forces that can take advantage of the flexibility of the pore rim. This effectively increases the area of transport. This is partly responsible for the increased current at higher voltages. However, the main cause of the latter is the chaperoning of ions across the pore by polarized water, which happens at lower voltage for K^+ compare to Cl^- due to the charge layer of the former being closer to the graphene membrane, see Fig. S-3(a).

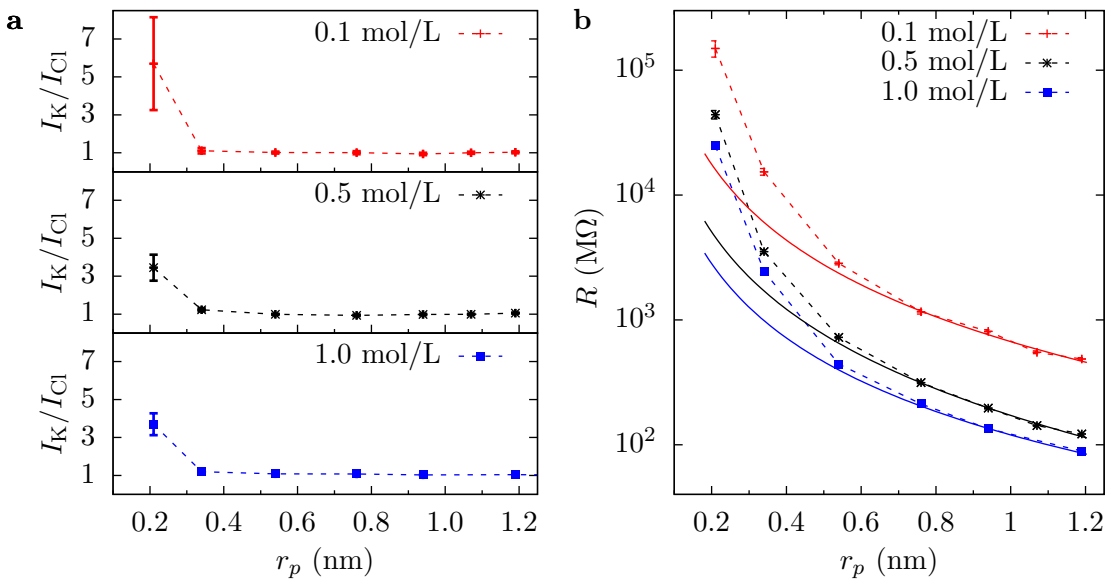

FIG. S-7. Selectivity and pore resistance for three different concentrations. (a) Selectivity and (b) pore resistance for 0.1 mol/L, 0.5 mol/L, and 1.0 mol/L KCl. The solid line is the fit of resistance of the form, $R = \frac{a}{r_p} + \frac{b}{r_p^2}$ [16, 17]. Here, the $1/r_p$ term is due to access resistance and the $1/r_p^2$ term is due to the pore resistance. Note that this deviation from normal behavior is quite large as the axis is on a logarithmic scale. The persistence of selectivity and the sharp rise in pore resistance at lower concentrations confirms that the behavior is not due to ion-ion interactions or some other many-body effect. Connecting lines are shown as a guide to the eye.

VI. TABLES

r_p (nm)	0.21	0.34	0.54	0.76	0.94	1.19	1.39	1.83	2.36
l (nm)	3.7	3.7	3.7	3.7	3.7	7.4	7.4	7.4	7.4
I_{K} (nA)	0.032	0.23	1.13	2.40	3.57	5.7	8.1	13.6	21.8
I_{Cl} (nA)	0.009	0.17	1.13	2.32	3.61	5.5	8.0	13.9	20.8
$I_{\mathrm{K}}/I_{\mathrm{Cl}}$	3.7	1.3	1.0	1.0	1.0	1.0	1.0	1.0	1.0

TABLE S-5. Current for various radii. The table shows the current for 1.0 mol/L KCl solution for the box of height $h = 6.9$ nm for various radii. The edge of the box is $l = b = 7.4$ nm for larger pores ($r_p > 1$ nm) and $l = b = 3.7$ nm for smaller pores. The latter allows for much longer simulations, which are needed to achieve convergence. The error in the current is shown in Fig. 2 in the main text. The block standard error determines the number of significant digits in this and the following tables.

V (V)	0.25	0.5	0.75	1.0	1.25	1.5	1.75	2.0	2.25	2.5	2.75	3.0
I_{K} (pA)	2.3	7.0	15	32	52	87	113	153	167	197	210	234
I_{Cl} (pA)	1.0	2.2	4.5	9	12	15	16	17	21	29	41	55
$I_{\mathrm{K}}/I_{\mathrm{Cl}}$	2.3	3.0	3.2	3.7	4.4	5.6	7.1	9.1	8.0	6.8	5.1	4.2

TABLE S-6. Current for various voltages. The table shows the current for 1.0 mol/L KCl solution through the smallest pore $r_p = 0.21$ nm for various voltages. For these calculations, we use the box height $h = 6.9$ nm and the smaller cross section, $l = b = 3.7$ nm. The error in the current is shown in Fig. S-6

	pore		bulk	
	$\langle p_r \rangle$ (D)	$\langle n \rangle$	$\langle p_r \rangle$ (D)	$\langle n \rangle$
K^+	2.02	5.2	1.60	6.8
Cl^-	1.81	5.8	1.54	7.4

TABLE S-7. Dipole orientation. The average radial component of individual water dipole $\langle p_r \rangle$ and average number of water dipoles $\langle n \rangle$ in the first hydration layer of K^+ an Cl^- ions in the smallest pore ($r_p = 0.21$ nm) and in the bulk. The dipole moment of water in our model is 2.35 in units of Debye (0.021 e nm). The dipoles are strongly oriented in the pore compare to bulk but have fewer dipoles and hence there is a decrease in total dipole moment.

Atoms (X)	K	Cl	H	O	C
ϵ_X (meV)	3.773	6.505	1.89	6.596	3.036
r_X (nm)	0.176	0.227	0.022	0.177	0.199

TABLE S-8. Lennard-Jones parameters for individual elements. The vdW potential between two atoms at a distance d, is calculated using the Lennard-Jones relation, $V_{\mathrm{LJ}} = \epsilon_m \left[\left(\frac{r_m}{d}\right)^{12} - 2\left(\frac{r_m}{d}\right)^{6} \right]$, where the parameter $r_m = r_1 + r_2$ is the equilibrium distance and $\epsilon_m = \sqrt{\epsilon_1 \epsilon_2}$ is the well depth of the interaction.

[1] Phillips, J. C. *et al.* Scalable molecular dynamics with NAMD. *J. Comput. Chem.* **26**, 1781–1802 (2005).

[2] Darden, T., York, D. & Pedersen, L. Particle mesh ewald: An n-log (n) method for ewald sums in large systems. *J. Chem. Phys.* **98**, 10089–10092 (1993).

[3] Martyna, G. J., Tobias, D. J. & Klein, M. L. Constant pressure molecular dynamics algorithms. *J. Chem. Phys.* **101**, 4177–4189 (1994).

[4] Darve, E., Rodríguez-Gómez, D. & Pohorille, A. Adaptive biasing force method for scalar and vector free energy calculations. *J. Chem. Phys.* **128**, 144120 (2008).

[5] Hénin, J. & Chipot, C. Overcoming free energy barriers using unconstrained molecular dynamics simulations. *J. Chem. Phys.* **121**, 2904–2914 (2004).

[6] Grossfield, A. & Zuckerman, D. M. Quantifying uncertainty and sampling quality in biomolecular simulations. *Annu. Rep. Comput. Chem.* **5**, 23–48 (2009).

[7] O'Hern, S. C. *et al.* Selective ionic transport through tunable subnanometer pores in single-layer graphene membranes. *Nano Lett.* **14**, 1234–1241 (2014).

[8] Aksimentiev, A. & Schulten, K. Imaging α-hemolysin with molecular dynamics: ionic conductance, osmotic permeability, and the electrostatic potential map. *Biophys. J.* **88**, 3745–3761 (2005).

[9] Zwolak, M., Wilson, J. & Di Ventra, M. Dehydration and ionic conductance quantization in nanopores. *J. Phys.: Condens. Matter* **22**, 454126 (2010).

[10] Ahn, S. & Fessler, J. A. Standard errors of mean, variance, and standard deviation estimators. *EECS Department, The University of Michigan* 1–2 (2003).

[11] Garaj, S. *et al.* Graphene as a subnanometre trans-electrode membrane. *Nature* **467**, 190–193 (2010).

[12] Hille, B. *Ion channels of excitable membranes*, vol. 507 (Sinauer Sunderland, MA, 2001).

[13] Bhattacharya, S. *et al.* Rectification of the Current in α-Hemolysin Pore Depends on the Cation Type: The Alkali Series Probed by Molecular Dynamics Simulations and Experiments. *J. Phys. Chem. C* **115**, 4255–4264 (2011).

[14] Jain, T. *et al.* Heterogeneous sub-continuum ionic transport in statistically isolated graphene nanopores. *Nat Nanotechnol* **10**, 1053–1057 (2015).

[15] Rollings, R. C., Kuan, A. T. & Golovchenko, J. A. Ion selectivity of graphene nanopores. *Nat. Commun.* **7**, 11408 (2016).

[16] Hall, J. E. Access reistance of a small circular pore. *J. Gen. Physiol.* **66**, 531–532 (1975).

[17] Schneider, G. F. *et al.* DNA translocation through graphene nanopores. *Nano Lett.* **10**, 3163–3167 (2010).